Cement & Concrete Composites 45 (2014) 255–263

Contents lists available at ScienceDirect

Cement & Concrete Composites

journal homepage: www.elsevier.com/locate/cemconcomp

3D spatial distribution of the calcium carbonate caused by carbonation of cement paste

Keshu Wan [a,b,*], Qiong Xu [b], Yudong Wang [b], Ganghua Pan [a,b]

[a] Jiangsu Key Laboratory of Construction Materials, Nanjing 211189, People's Republic of China
[b] School of Materials Science and Engineering, Southeast University, Nanjing 211189, People's Republic of China

ARTICLE INFO

Article history:
Received 26 March 2013
Received in revised form 23 July 2013
Accepted 9 October 2013
Available online 22 October 2013

Keywords:
Cement-based materials
Carbonation
Calcium carbonate
Tomography

ABSTRACT

Carbonation of cement-based materials is one area of concern for the durability of concrete structures. The calcium carbonate caused by carbonation is an important indicator of carbonation degrees. The present paper, using 3D tomography data, proposes a nondestructive method to characterize the 3D spatial distributions of calcium carbonate. It allows monitoring of 3D carbonation evolutions. The evolution of the calcium carbonate distributions in a specimen of cement paste with different carbonation degrees is given using the current method. The results are compared with the average quantity of calcium carbonate determined by thermal analysis. From the sharp edge of the calcium carbonate distribution, we conclude that the accelerated carbonation in this experimental condition is a diffusion controlling process.

1. Introduction

Cement-based materials are widely used in construction structures. Carbonation is one of the key factors influencing the durability of cement-based materials, as it can reduce the quality of the concrete that protects steel reinforcements from corrosion [1–4]. The carbonation process advances through several stages. Gaseous CO_2 first penetrates into the cement matrix, then it dissolves in the pore solution to produce CO_3^{2-} ions. Once CO_3^{2-} is in the pore solution, it is free to react with Ca^{2+} from calcium hydroxide (CH) to precipitate carbonate phases [1]. Calcite is regarded as the main reaction product of carbonation, although aragonite and valerite forms of calcium carbonate ($CaCO_3$) have also been reported [4,5]. The reactions cause a drop in pH of the pore solution, which leads to a dissolution of CH. Besides the CH carbonation, the interlayer calcium from calcium silicate hydrates (C–S–H) also reacts with CO_2 to form $CaCO_3$ [6]. The formation of $CaCO_3$ in replacement of CH is one of the main outcome of carbonation, and results in the carbonation depth. Experimental evidence of CH reduction upon $CaCO_3$ formation has been reported [7–9]. Accordingly, experimental quantification of the $CaCO_3$ or carbonation degree is important for research on carbonation of cement-based materials.

Different techniques have been used to quantify the $CaCO_3$ and the carbonation depth over the years [4,7,10–16]. Carbonation depth is typically measured using a phenolphthalein solution (such as in [4,7,10]), which is an indirect measure since the colorless indicator shows where the pH has dropped below approximately 9. In fact, this test method does not indicate the depth of maximum ingress of CO_2. Recent results show that this technique gives only an approximate estimation of the depth of carbonation. Using a method comparable to the acid-dissolution approach for chloride profile measurements, Houst and Wittmann [11] have shown that the carbonate fronts advance well beyond the depth indicated by phenolphthalein solution. DTA and TGA are intensively applied to quantify CH and C–S–H (such as in [12,13]). XRD has been used to study the different phases in carbonation [12–14]. As well, infrared spectroscopy (IR) [14] and Raman spectroscopy [15,16] have been applied to assess carbonation products in cement-based materials. None of these traditional methods can give the spatial distributions of $CaCO_3$ or quantitative carbonation profiles, which are significant for understanding the carbonation mechanism and for model verifications. Moreover, these methods are destructive in sample preparations.

Some NDE methods using X-rays or gamma-rays can give the spatial distribution of microstructure and even carbonation degrees. On the one hand, X-ray computer tomography (CT), which can observe the 3D structure directly without sample preparation, has been employed for scanning cement-based materials [17–28]. It has been used to deal with the problems of cement hydration and microstructure [17–20], calcium leaching [21–25], fracture [26,27], and carbonation [28] etc. For carbonation research [28],

* Corresponding author at: Jiangsu Key Laboratory of Construction Materials, Nanjing 211189, People's Republic of China. Tel.: +86 25 52090670; fax: +86 25 52090667.
E-mail address: keshuwan@seu.edu.cn (K. Wan).

0958-9465/$ - see front matter © 2013 Elsevier Ltd. All rights reserved.
http://dx.doi.org/10.1016/j.cemconcomp.2013.10.011

Han et al. have noticed the grayscale value (GSV) differences in the tomography image of partly carbonated cement pastes, while they did not study it thoroughly for quantitative $CaCO_3$ distributions. On the other hand, Villain et al. have measured the quantitative carbonation profiles using the gamma-ray absorption method [7,29–32]. Similar to the X-ray CT method, the gamma-ray absorption method is non-destructive such that the method can monitor the evolution of the carbonation process as a function of time on the same specimen. While the main limitation of the gamma-ray method is that only 1D information is obtained, the obtained 1D carbonation profile is the average result of the 3D distributions.

In this study, based on 3D X-ray CT data, an NDE method is proposed to characterize the 3D spatial distribution of $CaCO_3$ in partially carbonated cement-based materials. The carbonated $CaCO_3$ distributions in a specimen of cement paste with different carbonation degrees are given using the proposed method, and the results are further compared with the average quantity of $CaCO_3$ determined by thermal analysis.

2. Methods

The proposed method is mainly based on X-ray CT images. The principle of X-ray CT imaging has been discussed extensively, and the reconstructed CT image is a spatial distribution of the linear attenuation coefficients expressed by GSV, with brighter regions corresponding to higher values of the coefficient and darker regions to lower ones [33,34]. The principle of the proposed method is mainly based on the additivity of X-ray linear attenuation coefficients or partial volume effect, that is, the measured attenuation coefficient of any voxel is a weighted average of the values of each component material in the voxel. The principle will be explained in detail using the following illustration (Fig. 1) and physical equations.

As illustrated in Fig. 1, before carbonation, cement paste can be arbitrarily divided into three parts: (a) the carbonatable calcium expressed in the form of calcium hydroxide with a volume fraction of f^0_{CH} (includes not only the pure portlandite phase but also other calcium in cement matrix, such as the calcium in C–S–H or in unhydrated clinker); (b) the initial porosity with a volume fraction of; and (c) with the volume fraction of $1 - f^0_{CH} - \phi^0$. According to the additivity of linear attenuation coefficient, the linear attenuation coefficient of a voxel before carbonation μ_{before} can be expressed by

$$\mu_{before} = \mu_{CH} f^0_{CH} + \mu_{air}\phi^0 + \mu_{others}(1 - f^0_{CH} - \phi^0) \quad (1)$$

where μ_{CH}, μ_{air}, and μ_{others} are the linear attenuation coefficients of CH, air or water, and the other part stated in Fig. 1 respectively. Because the saturation degrees are hard to control, some pores filled with water and some pores filled with air. Fortunately, the linear attenuation coefficients of air and water are much smaller than that of the solid components, such as, CH or $CaCO_3$. Taking a 15 kV monochromatic X-ray as an example, the linear attenuation coefficients of air, water, and CH are 0.002, 1.68, and 37.91 cm^{-1} [19]. So the influence of air or water, or the influence of saturation, can be reasonably discarded, and only one μ_{air} parameter is used to express the linear attenuation coefficients of air or water in Eq. (1).

After carbonation, solid calcium is partly carbonated from the form of calcium hydroxide (mainly portlandite) to $CaCO_3$. Because calcite is generally identified as the main reaction product of carbonation [4,5,7,9], and it has a higher molar volume (36.9 cm^3/mol) compared to that of portlandite (33.1 cm^3/mol) [2], the formation of calcite in replacement of portlandite reduces the porosity of the material. Using the volume difference between portlandite and calcite to approximately express the volume variation due to carbonation, a reduced porosity of $\Delta\phi = \frac{38}{369} f_{CaCO_3}$ will be introduced, where f_{CaCO_3} is the volume fraction of $CaCO_3$. While, carbonation product will fill some pores at the micro-scale, at the same time, carbonation will cause some contractions. We suppose that the volume variation due to carbonation at the macro-scale can be neglected here; this will be verified from the image registration results in Section 4.2. Accordingly, the volume fraction of the un-carbonated calcium f_{CH} can be expressed by

$$f_{CH} = f^0_{CH} - f_{CaCO_3} + \Delta\phi \quad (2)$$

After partial carbonation, the linear attenuation coefficient of the voxel μ_{after} can be expressed as

$$\mu_{after} = \mu_{CH} f_{CH} + \mu_{CaCO_3} f_{CaCO_3} + \mu_{air}(\phi^0 - \Delta\phi) + \mu_{others}(1 - f^0_{CH} - \phi^0) \quad (3)$$

where μ_{CaCO_3} is the linear attenuation coefficients of $CaCO_3$. Ignoring μ_{air}, and combining Eqs. (1)–(3), the volume fraction of $CaCO_3$ can be calculated as

$$f_{CaCO_3} = \frac{\mu_{after} - \mu_{before}}{\mu_{CaCO_3} - (1 - \frac{38}{369})\mu_{CH}} \quad (4)$$

Because Eqs. (1)–(4) stand for any voxel, considering the geometrical abscissas (x, y, z), we then have

$$f_{CaCO_3}(x,y,z) = \frac{\mu_{after}(x,y,z) - \mu_{before}(x,y,z)}{\mu_{CaCO_3} - (1 - \frac{38}{369})\mu_{CH}} \quad (5)$$

Further considering that the GSV of the CT image is proportional to the linear attenuation coefficients, and keeping the same tomography scan parameters, the proportional parameters are same for all scans, and the volume fraction of $CaCO_3$ can then be calculated from the GSV directly, that is

$$f_{CaCO_3}(x,y,z) = \frac{G_{after}(x,y,z) - G_{before}(x,y,z)}{G_{CaCO_3} - (1 - \frac{38}{369})G_{CH}} \quad (6)$$

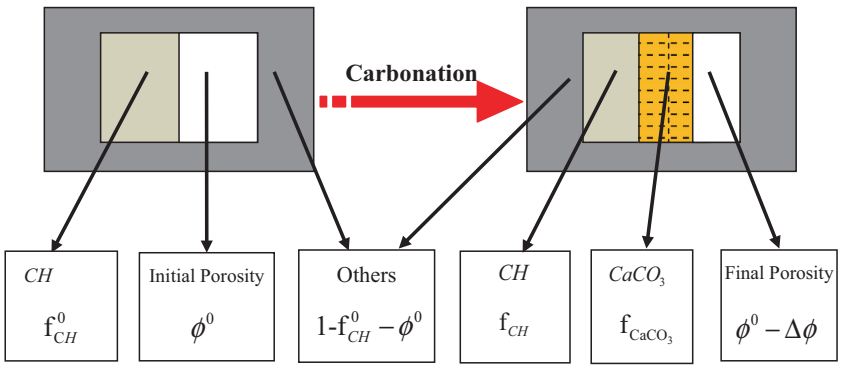

Fig. 1. Illustration of arbitrarily divided compositions and their volume fractions in any voxel before and after carbonation.

where $G_{before}(x,y,z)$ and $G_{after}(x,y,z)$ are the GSV of the specimen before and after carbonation at identical geometrical abscissas (x, y, z), and G_{CH} and G_{CaCO_3} are the GSV of portlandite and calcite respectively.

Because it is very hard to obtain large single crystals of portlandite and calcite, an indirect experimental method was used to measure G_{CH} and G_{CaCO_3}, which express respectively the linear attenuation coefficient of portlandite μ_{CH} and the linear attenuation coefficient of calcite μ_{CaCO_3}. Taking portlandite as an example, according to the additivity of the linear attenuation coefficient, if the porosity of a press bit of portlandite powder is known, then the linear attenuation coefficient of portlandite can be calculated from the averaged attenuation coefficient of that press bit $\overline{\mu_{CH-apparent}(x,y,z)}$. The porosity of a press bit of portlandite powder can be obtained from the apparent density and the theoretical density of portlandite, $1-\rho_{CH-apparent}/\rho_{CH}$. Using GSV to express the linear attenuation coefficient, we have:

$$G_{CH}=\frac{\overline{G_{CH-apparent}(x,y,z)}}{1-(1-\rho_{CH-apparent}/\rho_{CH})}=\frac{\overline{G_{CH-apparent}(x,y,z)}}{\rho_{CH-apparent}/\rho_{CH}} \tag{7}$$

Using the same process, G_{CaCO_3} can be experimentally obtained:

$$G_{CaCO_3}=\frac{\overline{G_{CaCO_3-apparent}(x,y,z)}}{\rho_{CaCO_3-apparent}/\rho_{CaCO_3}} \tag{8}$$

where $\overline{G_{CaCO_3-apparent}(x,y,z)}$ is the averaged GSV of the press bit of calcite powder crystals, $\rho_{CaCO_3-apparent}$ is the apparent density of the press bit of calcite powder, and ρ_{CaCO_3} is the theoretical density of calcite.

Experimentally, it is very hard to keep $G_{before}(x,y,z)$ and $G_{after}(x,y,z)$ at identical geometrical abscissas (x, y, z). A 3D image registration process [35,36] was thus applied to the CT data sets. For the 3D image registration of a rigid body, three translational freedoms and three rotational freedoms are sufficient. To take possible shrinkage into consideration, three scale freedoms are additionally considered in this research. The averaged squared difference of GSV at each voxel is used as the merit function for the 3D image registration. Through comparing the two 3D data sets, nine freedoms with least merit function value can be calculated, and then the image can be registered using the nine known freedoms. After the 3D image registration, Eq. (6) can be applied to calculate the $CaCO_3$ distribution using the CT data of the dual scans. The process of the method is illustrated in Fig. 2.

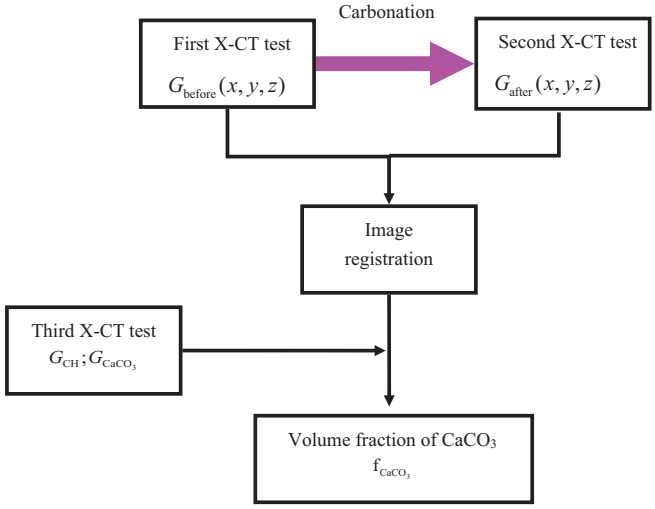

Fig. 2. Illustration of the method's process.

3. Experimental

3.1. Specimen preparation

The specimens were prepared with an ordinary Portland cement. A cement paste with a water-to-cement ratio of 0.53 was used, and the chemical composition of the cement is listed in Table 1. The specimens were cured in a standard curing room (temperature 20 ± 3 °C, relative humidity over 95%) for 28 days before the carbonation experiments.

The accelerated carbonation was applied at a CO_2 concentration of 20% and a temperature of 20 ± 2 °C with relative humidity of 70% ± 5%. The size of the prismatic specimen for carbonation was 40 mm × 40 mm × 100 mm. Before the accelerated carbonation, the specimen was placed in an oven at 50 °C for 48 h; four surfaces were then sealed with wax and only two parallel surfaces with a size of 40 mm × 100 mm were left for 1D carbonation.

The same specimen with different carbonation degrees was subjected to CT scans for three times: the first scan was run on the non-carbonated specimen, the second scan was run on the same specimen carbonated for 7 days, and the third scan was run on the same specimen carbonated for 14 (7 plus 7) days. After the third CT scan, the specimen carbonated for 14 days was destroyed for thermal analysis.

3.2. Tomography imaging

All tomography scans were performed using the YXLON micro-focus X-ray CT system (Y.CT Precision S, YXLON). The X-ray source is a 225 kV twin-head micro-focus source (Y.FXE 225.99), with a direct beam head and a transmission beam head. For the direct beam head used in our experiments, the minimum focus spot size is less than 3 μm. The detector is a flat panel detector (Y.XRD 0820) with a pixel number of 1024 × 1024 and a pixel size of 200 μm. Because of the cone beam magnification of 3.3 times, the effective pixel size is 60 μm. All scans were performed with X-ray peak energy at 195 kV and current at 0.3 mA. Each scan consisted of 1080 projections, with an acquisition time of 8 s per projection.

3.3. Thermal analysis

In the specimen for thermal analysis, hydration was stopped using alcohol exchange for 1 week first, and then the specimen was dried at 60 °C for 1 week. Powder samples were taken from depths of 0–3 mm, 4–6 mm, 8–12 mm and 13–17 mm to the carbonation surface respectively for thermal analysis.

The NETZSCH STA 449 F3 thermal analyzer was used for thermal analysis in the present study. It enabled the thermogravimetric (TG) curve and the differential thermal analysis (DTA) curve to be obtained simultaneously. A 0.3 g powder sample was heated from 25 °C to 1000 °C at a heating rate a 10 °C per minute under nitrogen gas protection. Mass fraction of $CaCO_3$ was calculated by its decomposition specific mass loss of CO_2 in the decomposition temperature range of 550–990 °C [7].

Table 1
Chemical composition of the cement/wt.%.

CaO	SiO_2	Al_2O_3	Fe_2O_3	MgO	SO_3	K_2O	Na_2O	LOI	Others
62.60	21.35	4.64	3.31	3.08	2.25	0.54	0.21	0.95	1.07

4. Results

4.1. Raw CT data

Although 1024 tomography slices with slice size of 1024 × 60 μm × 1024 × 60 μm were obtained from the CT tests, only 200 (12 mm) tomography slices in the center part of the specimen are analyzed. Before carbonation, GSV is relatively homogeneous aside from some large pores as shown in Fig. 3a and b. After 7 days or 14 days of carbonation, two main zones can be distinguished in Fig. 3c–f. A carbonated zone is clearly observed whose GSV is brighter than that of the sound zone in the center part. Because the attenuation coefficients increase after carbonation, it is reasonable to observe a brighter carbonated zone (brighter regions corresponding to higher values of the attenuation coefficient in CT images). This GSV difference between the sound zone and the carbonated zone is used for quantitative calculation of the volume fraction of $CaCO_3$ in this research.

Although we sealed four surfaces with wax to ensure 1D carbonation from only the two 40 mm × 100 mm surfaces (right and left surfaces in Fig. 3), it is interesting to note that the carbonation is not 1D carbonation at all. The observed carbonation fronts are not parallel to the carbonation surfaces; what is more, the carbonation fronts do not constitute a straight plane at all. In addition, several large cracks caused by carbonation are observed when comparing Fig. 5a and b with Fig. 5c–f. It is found that the

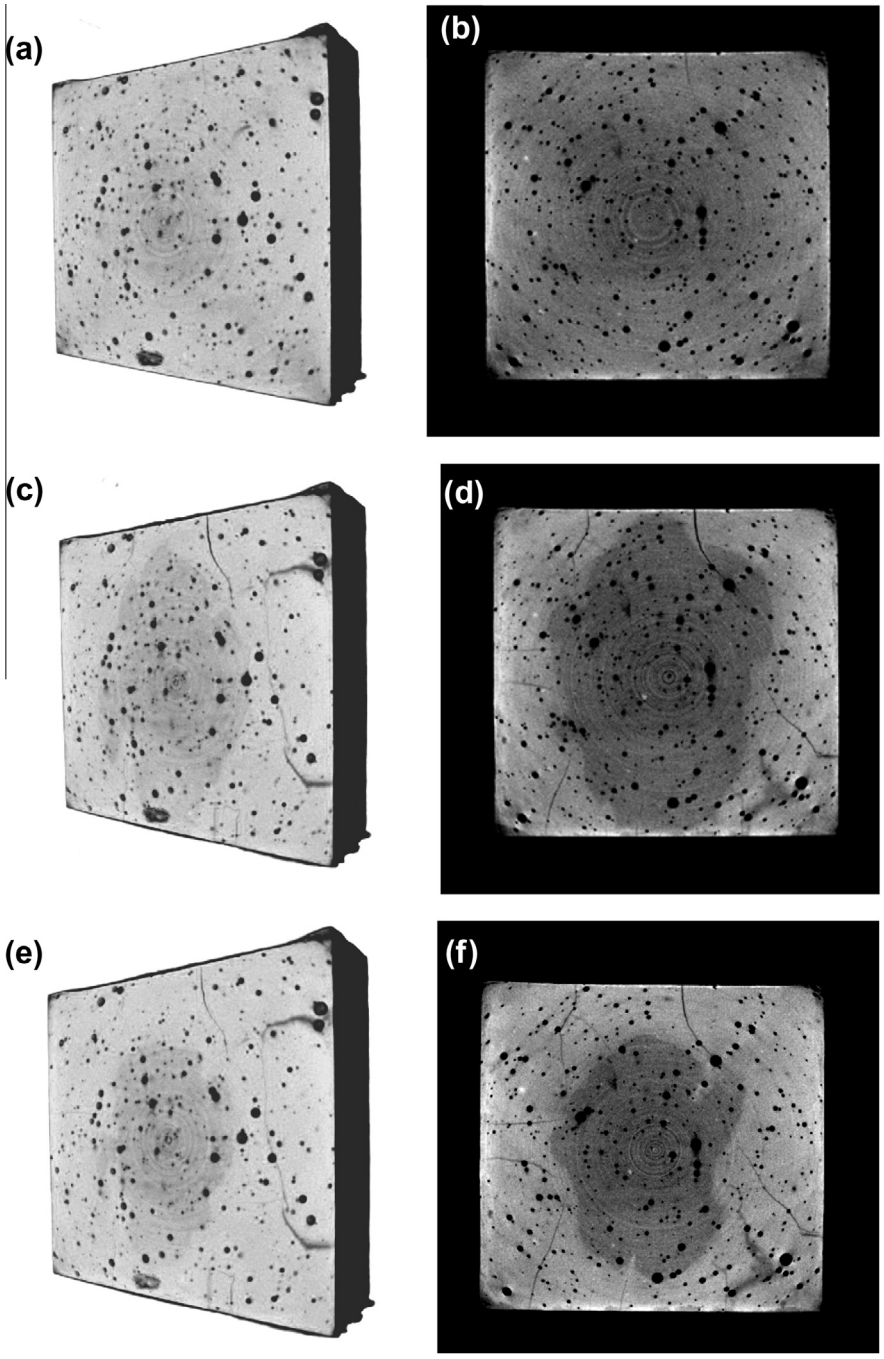

Fig. 3. (a) 3D rendering and (b) typical 2D slice of the sound specimen; (c) 3D rendering and (d) typical 2D slice of the specimen carbonated for 7 days; (e) 3D rendering and (f) typical 2D slice of the specimen carbonated for 14 days.

carbonation fronts go deeper around these cracks, so the carbonation cracks will further increase the carbonation process. It is believed that the cracks (both the observed large cracks and the unobservable micro-cracks) destroy the 1D carbonation. Considering that the cracks are hard to avoid during carbonation, true 1D carbonation is difficult to implement experimentally. It is thus hard to obtain a precise and straight carbonation plane experimentally.

4.2. Image registration

As the image registrations for the specimen before and after 7 or 14 days of carbonation are same, only the specimen after 14 days of carbonation is explained here. Without 3D image registration, it is very hard to find the identical matched slices of the specimen before and after 14 days of carbonation. Two typical slices with same height from the sample stage are compared in Fig. 4a and b, and the difference can be clearly distinguished. Algebraic operations using Eq. (6) cannot be applied directly on the two 3D data sets.

The 3D data set of the specimen carbonated for 14 days is registered with the 3D data set of the sound specimen. Three translational freedoms, three rotational freedoms, and three scale freedoms are calculated as −19.8810, −1.32162, −0.650638; 0.0500207, −0.518734, 0.727554; and 0.997754, 0.999032, 0.998203, respectively. The three scale freedoms are very close to 1, which means the macro-volume variation due to carbonation is negligible; the volume supposition in Section 2 is acceptable. The 3D image data set can be registered using the nine known freedoms, and one typical 2D slice of the registered 3D data corresponded to Fig. 4a is shown in Fig. 4c. The subtraction between Fig. 4a and c is shown in Fig. 4d, and a good registered result is clearly illustrated. Now algebraic operations using Eq. (6) can be applied directly to the two 3D data sets of the specimen before and after carbonation.

4.3. 3D distribution of $CaCO_3$

To calculate the 3D spatial distribution of $CaCO_3$ using Eq. (6), the GSV of polandite and calcite (G_{CH} and G_{CaCO_3}) are required. An indirect method described in the experimental part is applied. Using Eqs. (7) and (8) and the data shown in Table 2, the GSV of polandite G_{CH} and the GSV of calcite G_{CaCO_3} are calculated as 261 and 296 respectively.

3D $CaCO_3$ maps of cement pastes with different carbonation degrees are calculated according to Eq. (6) and are shown in Fig. 5. Although there is some noise, the carbonation fronts and the $CaCO_3$ distribution due to carbonation can be observed from the 3D $CaCO_3$ maps (Fig. 5a and b) and typical 2D $CaCO_3$ maps (Fig. 5c and d) of the specimen carbonated for 7 days and for 14 days. To further show the quantitative results of the 3D $CaCO_3$ maps, 1D $CaCO_3$ line profiles of the specimen carbonated for 7 days and 14 days are shown in Fig. 5e and f respectively. The most notable information is the sharp edge on both specimens with different carbonation degrees. The volume fractions of $CaCO_3$ for the carbonated zone are about 0.13 and 0.15 for the specimen carbonated for 7 days and for 14 days. The volume fraction of $CaCO_3$ in the sound region is about zero. A very sharp

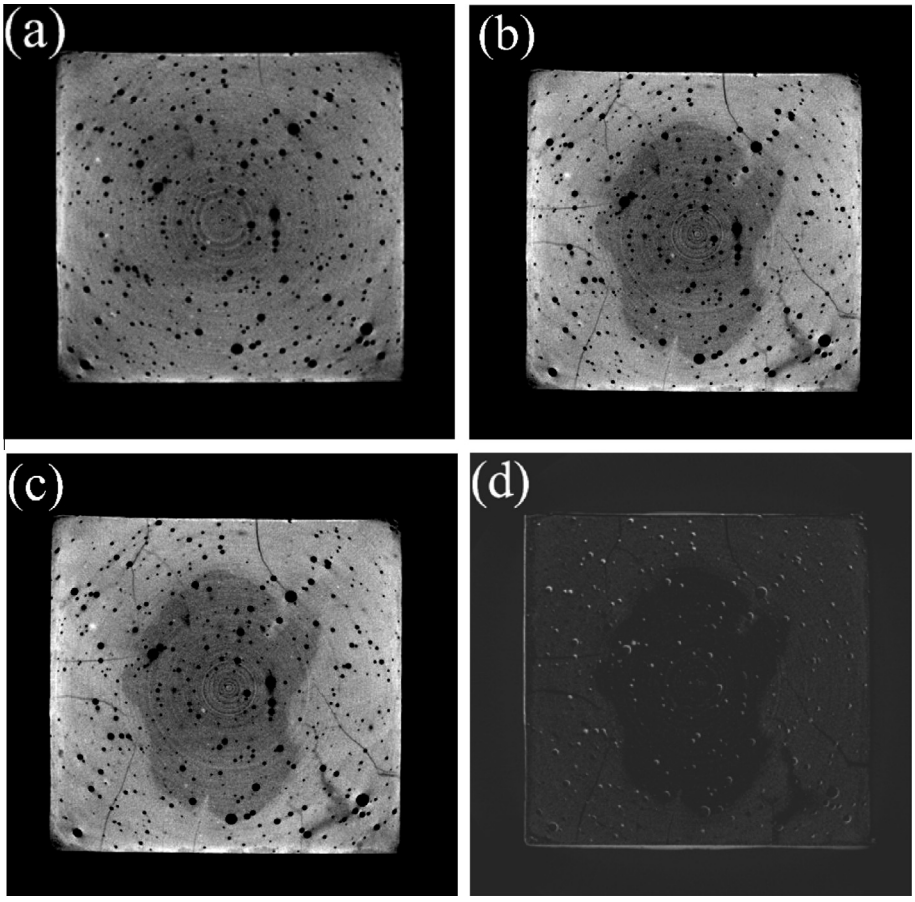

Fig. 4. Example slices showing the image registration results. (a) typical 2D slice of the sound specimen; (b) typical 2D slice of the carbonated specimen; (c) typical 2D slice of registered data; (d) the subtraction between (a) and (c).

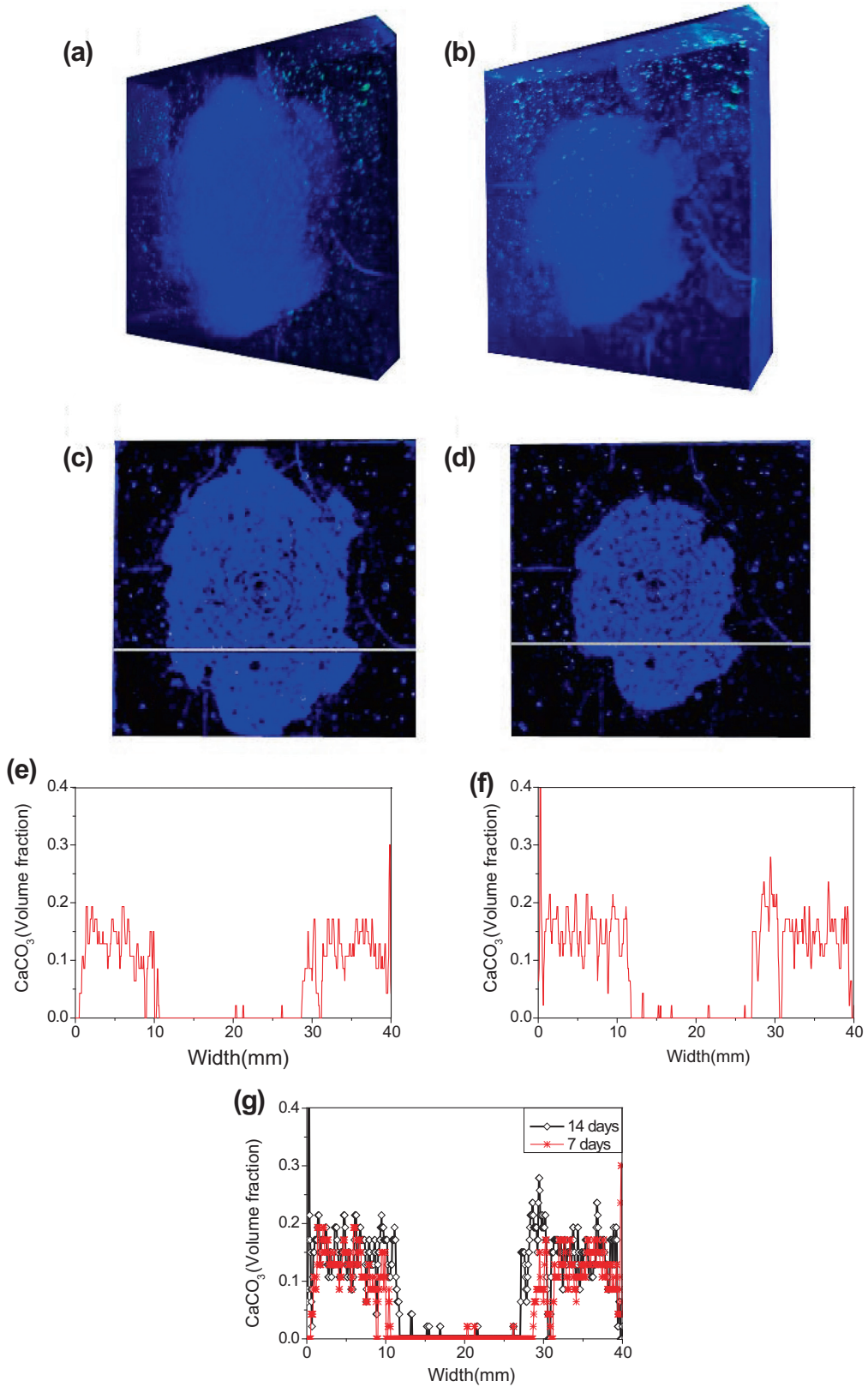

Fig. 5. Spatial distribution of the volume fraction of $CaCO_3$ for same specimen with different carbonation degrees: (a) 3D rendering of $CaCO_3$ map for the specimen carbonated for 7 days and (b) for 14 days; (c) typical 2D slice of the $CaCO_3$ map for the specimen carbonated for 7 days and (d) for 14 days; (e) 1D line profiles of the $CaCO_3$ map for the specimen carbonated for 7 days specimen and (f) for 14 days; (g) 1D $CaCO_3$line profiles on the same position of the specimen carbonated for 7 days and 14 days.

edge between the sound zone and the carbonated zone is observed. Different line profiles on different positions give similar information, which is not shown here.

Thanks to the registered 3D $CaCO_3$ maps, the carbonation depths and the volume fractions of $CaCO_3$ on the same position can be monitored at different carbonation periods. On the same po-

Table 2
Parameters to calculate the G_{CH} and G_{CaCO_3}.

	Mass (g)	Volume (cm^3)	$\rho_{apparent}$ (g/cm^3)	ρ (g/cm^3)	$\rho_{apparent}/\rho$	$\overline{G_{apparent}(x,y,z)}$	G
CH	13.1	10.5	1.25	2.24	0.56	146	261
$CaCO_3$	12.1	7.70	1.57	2.93	0.54	160	296

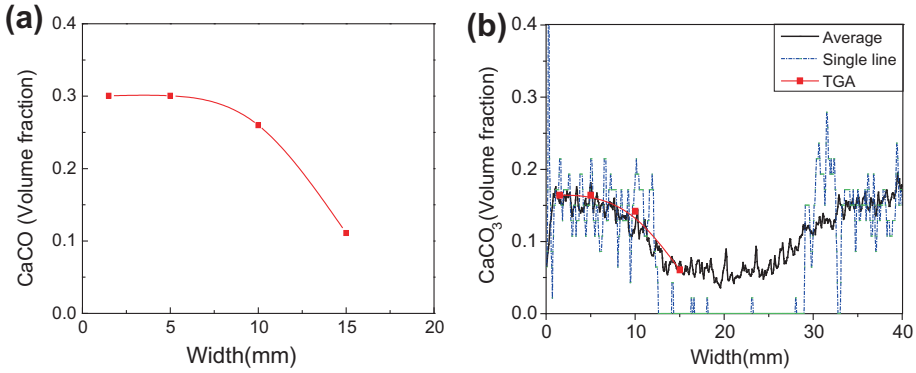

Fig. 6. (a) The weight fraction of $CaCO_3$ characterized by thermal analysis; (b) the volume fraction of $CaCO_3$ characterized by thermal analysis and the proposed tomography method: one line is the single line profile shown in Fig. 5(f), the other line is the average result on 3D volume.

sition, 1D $CaCO_3$ line profiles of the specimen carbonated for 7 days and for 14 days are drawn and shown in Fig. 5g, from which the evolution of the $CaCO_3$ distributions can be clearly observed. Firstly, the carbonation depth is different. Secondly, the volume fraction of $CaCO_3$ on the carbonated part is different, which means the quantity of $CaCO_3$ kept growing even behind the carbonation fronts.

4.4. Comparison with thermal analysis

Using thermal analysis method, the average mass fraction of $CaCO_3$ of the analyzed sample can be characterized. Powder samples for thermal analysis were taken from the specimen carbonated for 14 days at a depth of 0–3 mm, 4–6 mm, 8–12 mm and 13–17 mm from the carbonation surface, and the distribution of $CaCO_3$ (mass fraction) is shown in Fig. 6a. To compare it with the distribution of the volume fraction from the proposed method, the mass fraction is changed to volume fraction using densities of the dry specimen (1.60 g/cm^3) and calcite (2.93 g/cm^3) respectively, as shown in Fig. 6b. Because the volume fraction of $CaCO_3$ obtained from the thermal analysis method is an average result, we take the average of the tomography results on 3D volume to compare them with the thermal analysis results. Both the average line profile on 3D volume and the single line profile are shown in Fig. 6b. From the 1D spatial distribution of $CaCO_3$, it is found that the volume fraction of the average results using the tomography method shows a good match with the thermal analysis results. Through comparing the single line profile and the average line profile of $CaCO_3$, it is found that the sharp carbonation front is greatly smoothened by the averaging process.

5. Discussion

5.1. Advantages and limitations of the current method

The advantages of the proposed method are as following:

Firstly, the current method is nondestructive, which makes it possible to carry out measurements without disturbing the chemical composition. Because the accelerated carbonation is stopped only during a few hours, it is possible to monitor the evolution of the $CaCO_3$ distributions on the same cement paste with different carbonation degrees. Moreover, CT measurement can be performed in parallel with other techniques, such as XRD, phenolphthalein indicator spraying, and thermal analysis.

Secondly, thanks to the 3D tomography, the current method can give the 3D spatial distributions of $CaCO_3$. 3D carbonation information has several benefits. First of all, the 3D distributions of $CaCO_3$ presented here have more credibility than the averaged 2D or 1D carbonation profiles, which will be further explained in the next section. Moreover, the relation among 1D carbonation, 2D carbonation, and 3D carbonation can be investigated using the current method. Last but not least, the influences of cracks on carbonation can be directly investigated using the current method.

Thirdly, although only cement paste specimens were investigated using the proposed method, the method can also be applied to mortar and concrete specimen. Generally, carbonation has no influence on sand and aggregate, and only the attenuation coefficient (GSV of CT images) of cement matrix is altered. Because sand or aggregate does not influence the principle of the method, the method can be applied to all kinds of cement-based materials.

The proposed method also has its limitations. Firstly, because two CT scans on same specimen before and after carbonation are required, the provided method can only be applied on accelerated carbonation. For natural carbonation, the long carbonation period is not practical for CT scans. While considering that accelerated methods are intensively used for durability research, the present method still has its meaning. Secondly, we assume that calcite is the predominant form of $CaCO_3$ present in the carbonated specimens according to Refs. [4,5,7,9] and ignore the influences of aragonite and vaterite, while we cannot exclude the possibility of the presence of aragonite and vaterite in the carbonated specimens under different carbonation conditions. If some aragonite and vaterite do form during carbonation, both attenuation coefficient and molar volume of other phases are different with that of calcite, so the denominator of Eq. (6) is altered. This is one of the main shortcomings of the proposed method, and it will cause some errors.

5.2. Discussion on the sharp front

There is still some debate as to whether the carbonation is a pure CO_2-diffusion controlling process or a diffusion and reaction

controlling process (such as in [3,4,7,11,37–39]). From the modeling viewpoint, it has been shown that the width of the carbonation front is directly governed by the carbonation reaction time or the CO_2-diffusion time [4,7]. When the chemical reaction is instantaneous (diffusion controlling process), the width of the carbonation front is very sharp. When the reaction time is comparable with the diffusion time (diffusion and reaction controlling process), the width of carbonation front is much broader. Whether the carbonation front is sharp or not is extremely important for understanding the carbonation mechanism and for modeling research. Experimentally, some studies have observed gradual carbonation fronts (such as in [7,11,30,31,38,39]), which implies that carbonation is a diffusion and reaction controlling process. As explained in the introduction, normal methods can only obtain average information on the carbonation front, so the observed shallow fronts using traditional average methods can not reflect the real carbonation front.

In our research, the 3D distributions of $CaCO_3$ in Fig. 5 reveal a very sharp carbonation front. Considering that the 1D carbonation profiles obtained from traditional methods (including TGA analysis and the gamma-ray method) were just average results over the whole 3D carbonation distributions, the real carbonation profiles would inevitably be smoothened. The averaging effect has been illustrated in Fig. 5 and Fig. 6, so the 3D distributions of $CaCO_3$ presented here have more credibility. From the sharp carbonation fronts, we deduce that the accelerated carbonation in our experimental conditions is a diffusion controlling process.

Because carbonation is a very complicated process, which is influenced by many experimental and material conditions [39,40], we are not sure that all carbonations are diffusion controlled. More research on the 3D carbonation profiles on different carbonation conditions and using different materials is required to clarify this point. Of course, even if the carbonation is a diffusion and reaction controlling process in some other cases, the 3D spatial distribution of $CaCO_3$ still can be experimentally determined using the proposed method. Besides cement paste, the proposed method can be easily applied to other cement-based materials, such as mortars and concretes.

6. Conclusions

Based on tomography data, we propose a method to characterize the 3D spatial distributions of $CaCO_3$ due to carbonation in this research, and the $CaCO_3$ distributions in the cement paste specimen carbonated for 7 days and for 14 days are given using the proposed method. The results are compared with the average quantity of $CaCO_3$ determined by thermal analysis.

The proposed NDE method is powerful. Firstly, it can give 3D carbonation distribution which is not detectable by the traditional analysis methods. Secondly, it is nondestructive so that monitoring of carbonation evolution on same specimen is possible. Thirdly, it can be applied to carbonation research of all kinds of cement-based materials, including cement pastes, mortars, and concretes. Two limitations of the method need to be noted. Firstly, the method can only be applied on accelerated carbonation. Secondly, the calcite assumption maybe not hold on some special carbonation conditions.

The proposed method can be used not only for experimental research, but also for modeling verifications. Using the 3D $CaCO_3$ distributions determined by the method, more and deeper understanding of the carbonation mechanism of cement-based materials can be anticipated. Such as, the accelerated carbonation in this experimental condition is deduced to be a diffusion controlling process from the sharp edge of $CaCO_3$ distribution. They will contribute to better model the carbonation process and thus to be able to predict the service life of infrastructures under carbonation attack.

Acknowledgements

This research was sponsored by the foundation of the National Basic Research Program of China (No. 2009CB623203) and the National Natural Science Foundation of China (Nos. 51178103 and 51008072).

References

[1] Parrott LJ. A review of carbonation in reinforced concrete. Cement and concrete association. Great Britain: Wexham Springs; 1987.
[2] Glasser FP, Marchand J, Samson E. Durability of concrete-degradation phenomena involving detrimental chemical reactions. Cem Concr Res 2008;38:226–46.
[3] Burkan Isgor O, Razaqpur AG. Finite element modeling of coupled heat transfer, moisture transport and carbonation processes in concrete structures. Cem Concr Compos 2004;26(1):57–73.
[4] Papadakis VG, Vayenas CG, Fardis MN. Fundamental modeling and experimental investigation of concrete carbonation. ACI Mater J 1991;88(4):363–73.
[5] Saetta AV, Schrefler BA, Vitaliani RV. The carbonation of concrete and the mechanism of moisture, heat and carbon dioxide flow through porous materials. Cem Concr Res 1993;23(4):761–72.
[6] Gervais C, Garrabrants AC, Sanchez F, Barna R, Moszkowicz P, Kosson DS. The effects of carbonation and drying during intermittent leaching on the release of inorganic constituents from a cement-based matrix. Cem Concr Res 2004;34(1):119–31.
[7] Thiery M, Villain G, Dangla P, Platret G. Investigation of the carbonation front shape on cementitious materials: effects of the chemical kinetics. Cem Concr Res 2007;37(7):1047–58.
[8] Rigo da Silva CA, Reis RJP, Lameiras FS, Vasconcelos WL. Carbonation-related microstructural changes in long-term durability concrete. Mater Res 2002;5(3):287–93.
[9] Cultrone G, Sebastian E, Huertas MO. Forced and natural carbonation of lime-based mortars with and without additives mineralogical and textural changes. Cem Concr Res 2005;35(12):2278–89.
[10] Lo Y, Lee HM. Curing effects on carbonation of concrete using a phenolphthalein indicator and Fourier-transform infrared spectroscopy. Build Environ 2002;37(5):507–14.
[11] Houst YF, Wittmann FH. Depth profiles of carbonates formed during natural carbonation. Cem Concr Res 2002;32(12):1923–30.
[12] Cole WF, Kroone B. Carbon dioxide in hydrated Portland cement. J Am Concrete Inst Proc 1960;56(6):1275–95.
[13] Borges PHR, Costa JO, Milestone NB, Lynsdale CJ, Streatfield RE. Carbonation of CH and C–S–H in composite cement pastes containing high amounts of BFS. Cem Concr Res 2010;40(2):284–92.
[14] Fernandez-Carrasco L, Torrens-Martin D, Martinez-Ramirezb S. Carbonation of ternary building cementing materials. Cem Concr Compos 2012;34(10):1180–6.
[15] Martinez-Ramirez S, Sanchez-Cortes S, Garcia-Ramos JV, Doming C, Fortes C, Blanco-Varela MT. Micro-Raman spectroscopy applied to depth profiles of carbonates fromed in lime mortar. Cem Concr Res 2003;33(12):2063–8.
[16] Black L, Breen C, Yarwood J, Garbev K, Stemmermann P, Gasharova B. Structural features of C–S–H and its carbonation in air – a Raman spectroscopic study. Part II: Carbonated phases. J Am Ceram Soc 2007;90(3):908–17.
[17] Bentz DP, Quenard DA, Kunzel HM, Baruchel J, Peyrin F, Martys NS, et al. Microstructure and transport properties of porous building materials. II: Three-dimensional X-ray tomographic studies. Mater Struct 2000;33(3):147–53.
[18] Bentz DP, Mizell S, Satterfield S, Devaney J, George W, Ketcham P, et al. The visible cement data set. J Res NIST 2002;107(2):137–48 [See also http://www.visiblecement.nist.gov].
[19] Promentilla MAB, Sugiyama T, Hitomi T, Takeda N. Characterizing the 3D pore structure of hardened cement paste with synchrotron microtomography. J Adv Concr Technol 2008;6(2):273–86.
[20] Chotard TJ, Boncoeur-Martel MP, Smith A, Dupuy JP, Gault C. Application of X-ray computed tomography to characterize the early hydration of calcium aluminate cement. Cem Concr Compos 2003;25(1):145–52.
[21] Sugiyama T, Promentilla MAB, Hitomi T, Takeda N. Application of synchrotron microtomography for pore structure characterization of deteriorated cementitious materials due to leaching. Cem Concr Res 2010;40(8):1265–70.
[22] Burlion N, Bernard D, Chen D. X-ray microtomography: application to microstructure analysis of a cementitious material during leaching process. Cem Concr Res 2006;36(2):346–57.
[23] Rougelot T, Burlion N, Bernard D, Skoczylas F. About microcracking due to leaching in cementitious composites: X-ray microtomography description and numerical approach. Cem Concr Res 2010;40(2):271–83.

[24] Wan KS, Li Y, Sun W. Application of tomography for solid calcium distributions in calcium leaching cement paste. Constr Build Mater 2012;36:913–7.
[25] Wan KS, Li Y, Sun W. Experimental and modelling research of the accelerated calcium leaching of cement paste in ammonium nitrate solution. Constr Build Mater 2013;40:832–46.
[26] Landis EN, Zhang T, Nagy EN, Nagy G, Franklin WR. Cracking, damage and fracture in four dimensions. Mater Struct 2007;40(4):357–64.
[27] Landis EN. X-ray microtomography. Mater Char 2010;61(12):1305–16.
[28] Han JD, Sun W, Pan GH, Wang CH, Rong H. Application of X-ray computed tomography in characterization microstructure changes of cement pastes in carbonation process. J Wuhan Univ Technol Mater Sci Ed 2012;27(2):358–63.
[29] Villain G, Thiery M. Gamma densimetry: a method to determine drying and carbonation profiles in concrete. NDT&E Int 2005;39(4):328–37.
[30] Villain G, Platret G. Two experimental methods to determine carbonation profiles in concrete. ACI Mater J 2006;103(4):265–71.
[31] Villain G, Platret G. Comparison of two experimental methods to determine carbonation profiles in concrete. In: V.M. Malhotra, editor. Proceedings supplementary papers of the 6th CANMET/ACI international conference on durability of concrete. Thessaloniki, Greece; 2003. p. 179–94.
[32] Villain G, Thiery M, Platret G. Measurement methods of carbonation profiles in concrete: thermogravimetry. Cem Concr Res 2007;37(8):1182–92.
[33] Hounsfield GN. Computerized transverse axial scanning (tomography), 1. Description of system. Brit J Radiol 1973;46(552):1016–22.
[34] Kalender WA. Computed tomography: fundamentals, system technology, image quantity, applications. Weinheim: Wiley-VCH; 2000.
[35] Ketcham RA, Iturrino GJ. Nondestructive high-resolution visualization and measurement of anisotropic effective porosity in complex lithologies using high-resolution X-ray computed tomography. J Hydrol 2005;302(1–4):92–106.
[36] Fukuda D, Nara Y, Kobayashi Y, Maruyama M, Koketsu M, Hayashi D, et al. Investigation of self-sealing in high-strength and ultra-low-permeability concrete in water using micro-focus X-ray CT. Cem Concr Res 2012;42(11):1494–500.
[37] Ortoleva P, Merino E, Moore C, Chadam J. Geochemical self organization I; Reaction-transport feedbacks and modeling approach. Am J Sci 1987;287(10):979–1007.
[38] Parrott LJ, Killoh DC. Carbonation in a 36 year old in-situ concrete. Cem Concr Res 1989;19(4):649–56.
[39] Rahman AA, Glasser FP. Comparative studies of the carbonation of hydrated cements. Adv Cem Res 1989;2(6):49–54.
[40] Da Silva FG, Helene P, Castro-Borges P, Liborio JB. Sources of variations when comparing concrete carbonation results. J Mater Civ Eng 2009;21(7):333–42.